

RESEARCH ARTICLE OPEN ACCESS

# Defect Engineering in Ti-Doped $Ta_3N_5$ Thin Films for Enhanced Photoelectrochemical Water Splitting: Electronic Structure Modulation and Charge Carrier Dynamics

Shailesh Kalal<sup>1</sup>  | Martin Magnuson<sup>1</sup>  | Alessandro Chesini<sup>2</sup>  | Akshaya A<sup>3</sup> | Sanath Kumar Honnali<sup>4</sup>  | Sophia Sahoo<sup>5</sup>  | Nakul Jain<sup>6</sup>  | Dibyendu Bhattacharyya<sup>7</sup>  | Andrei Gloskovskii<sup>8</sup> | Mukul Gupta<sup>3</sup>  | Feng Wang<sup>6</sup> | Michele Orlandi<sup>2</sup>  | Grzegorz Greczynski<sup>1</sup>  | Kenneth Järrendahl<sup>1</sup>  | Per Eklund<sup>1,4</sup>  | Jens Birch<sup>1</sup>  | Ching-Lien Hsiao<sup>1</sup> 

<sup>1</sup>Thin Film Physics Division, Department of Physics, Chemistry and Biology (IFM), Linköping University, Linköping, Sweden | <sup>2</sup>Physics Department, University of Trento, Trento, Italy | <sup>3</sup>UGC-DAE Consortium for Scientific Research, University Campus, Indore, India | <sup>4</sup>Inorganic Chemistry, Department of Chemistry - Ångström Laboratory, Uppsala University, Uppsala, Sweden | <sup>5</sup>MESA + Institute for Nanotechnology, University of Twente, Enschede, Netherlands | <sup>6</sup>Electronic and photonic materials, Department of Physics, Chemistry and Biology (IFM), Linköping University, Linköping, Sweden | <sup>7</sup>Atomic and Molecular Physics Division, Bhabha Atomic Research Centre, Mumbai, India | <sup>8</sup>Deutsches Elektronen-Synchrotron, DESY, Hamburg, Germany

**Correspondence:** Shailesh Kalal (shailesh.kalal86@gmail.com) | Ching-Lien Hsiao (ching-lien.hsiao@liu.se)

**Received:** 29 July 2025 | **Revised:** 22 October 2025 | **Accepted:** 4 November 2025

**Keywords:** charge compensation | defect engineering | HAXPES | nitride semiconductor | photoelectrocatalysis |  $Ta_3N_5$  | XAS

## ABSTRACT

Tantalum nitride ( $Ta_3N_5$ ) is a promising semiconductor for solar-driven photoelectrochemical (PEC) water splitting, but its performance is limited by intrinsic defects. Here, we investigate the effect of titanium (Ti) doping (0–10 at%) on the structural, compositional, and optoelectronic properties of  $Ta_3N_5$  thin films. At low concentrations (<2 at%),  $Ti^{4+}$  preferentially substitutes Ta at four-coordinated sites, enhancing nitrogen incorporation and suppressing defect states associated with under-coordinated Ta. This leads to improved carrier dynamics and prolonged electron–hole lifetimes. Higher doping levels ( $\geq 3.5$  at%) result in occupation of three-coordinated sites, inducing increase in the oxygen content, lattice distortion, and defect formation that deteriorate carrier lifetimes. PEC measurements reveal that optimized Ti doping significantly reduces charge transfer resistance and nearly seven-fold increase in the photocurrent. These findings underscore the importance of controlled Ti doping for defect engineering and band structure tuning to boost the PEC performance of  $Ta_3N_5$  thin films.

## 1 | Introduction

Photoelectrochemical (PEC) water splitting has emerged as a promising method for converting solar energy into chemical fuels such as hydrogen and oxygen [1–3]. The PEC process is particularly attractive due to the abundance of solar energy and water, along with the absence of harmful byproducts. By enabling efficient energy storage, PEC water splitting addresses both energy and environmental challenges [3, 4]. The performance of PEC

water splitting is fundamentally governed by the band structure of the semiconductor photoanode. Nearly 43% of the solar spectrum lies within the visible range (400–700 nm), making semiconductors with bandgaps in this range particularly effective for light absorption and solar energy conversion, while also ensuring appropriate band-edge positions for water oxidation and reduction. Titanium dioxide ( $TiO_2$ ) was the first widely studied material due to its excellent chemical stability and photocatalytic properties. However, its large band gap ( $\approx 3.2$  eV) restricts

This is an open access article under the terms of the [Creative Commons Attribution License](#), which permits use, distribution and reproduction in any medium, provided the original work is properly cited.

© 2025 The Author(s). *Small Structures* published by Wiley-VCH GmbH.

light absorption mainly to the ultraviolet (UV) region, necessitating the development of alternative materials with enhanced visible light absorption [5].

Recent research has been devoted to nitrides and oxynitrides such as  $Ta_3N_5$  [6],  $BaTaO_2N$  [7],  $LaTiO_2N$  [8], and  $SrTaO_2N$  [9], which exhibit suitable band-edge positions and relatively narrow band gaps. Among them,  $Ta_3N_5$ , an n-type semiconductor [10, 11], has gained substantial attention due to its optimal bandgap of 2.1–2.2 eV, theoretical saturation photocurrent density of  $12.6\text{ mA/cm}^2$ , and band positions that align well with the redox potential of water [6, 12–18]. These attributes make  $Ta_3N_5$  a promising candidate for PEC applications, with a theoretical solar-to-hydrogen (STH) conversion efficiency of 15.9% [16]. Furthermore, the flat band potential of  $Ta_3N_5$  is more negative than the water reduction potential, suggesting a low onset potential for water oxidation [15]. Despite such desirable properties, the PEC performance of  $Ta_3N_5$  remains limited by poor charge transport. Consequently, pure  $Ta_3N_5$  photoanodes often suffer from low photocurrent density, high onset potential, poor stability, and low photon-to-current efficiency. In response to these challenges, intensive research has been dedicated to exploring different ways to mitigate these limitations. For instance, Fu et al. [18] demonstrated a significant improvement in applied bias photon-to-current efficiency from 2.29% to 3.46% through heterostructure engineering, employing n-type In:GaN and p-type Mg:GaN as top and bottom interfaces of  $Ta_3N_5$ . Similarly, Pihosh et al. [16] reported a reproducible STH conversion efficiency of approximately 12%, achieved by suppressing optical and charge-carrier recombination in  $Ta_3N_5$  nanorods loaded with catalysts. Furthermore, Kwon et al. [19] showed a reduction in onset potential from 0.69 to 0.27 V by implementing Z-scheme charge transport in  $Ta_3N_5$  grown on Si, with  $NbN_x$  acting as an electron mediator and  $CoFeO_x$  as a cocatalyst. These studies highlight that the slow surface kinetics in  $Ta_3N_5$  can be effectively addressed through artificial heterostructure engineering [7, 14, 18].

Another significant challenge in  $Ta_3N_5$  is the presence of intrinsic point defects and impurities, which are difficult to control during synthesis and severely impact performance [16]. Typically,  $Ta_3N_5$  is synthesized by nitridation of tantalum oxide ( $TaO_x$ ) under ammonia atmosphere, a process that can introduce residual oxygen up to 10 at% resulting in unintended defects such as substitutional oxygen impurities at nitrogen sites ( $O_N$ ), nitrogen vacancies ( $v_N$ ), and reduced Ta states ( $Ta^{3+}$ ) [20]. Density functional theory (DFT) calculations suggest that  $O_N$  defects create shallow donor states, enhancing the n-type conductivity of  $Ta_3N_5$  and improving photogenerated current [21]. However, other studies indicate that  $O_N$  defects at  $Ta_3N_5$  interfaces hinder water adsorption, leading to a higher onset potential [12, 13, 22]. Additionally, deep-level trap states have been observed in  $Ta_3N_5$ , though their origin remains debated. Some reports attribute these states to conduction band (CB) electron trapping at reduced Ta centers, while others suggest they arise from  $v_N$  defects causing sub-band-gap absorption. These defects contribute to severe photocarrier trapping and recombination, ultimately degrading PEC performance [20]. Therefore, developing strategies to suppress or passivate these defect states is essential for improving the efficiency of  $Ta_3N_5$  photoanodes.

To mitigate challenges related to charge transport and trapping, various strategies have been explored, including optimizing synthesis conditions, fabricating nanostructures, and constructing layered heterojunctions [6, 14, 16–18, 23–28]. Among these, foreign atom doping has been extensively investigated, yielding significant performance enhancements and various range of dopants along with co-doping strategies have been studied. However, the impact of metal doping and oxygen impurities has varied across different studies. Seo et al. [29] introduced Mg-Zr co-doped  $Ta_3N_5$ , which exhibited a negative shift in the onset potential and an enhanced photocurrent. Subsequent theoretical studies confirmed that Zr doping induces a cathodic shift in the onset potential of  $Ta_3N_5$ , while Mg doping enhances the photocurrent. Experimental findings further suggest that Mg-Zr [30], Zr-Cu [31] co-doped  $Ta_3N_5$  significantly suppresses the formation of reduced Ta species. Recent DFT calculations and non-adiabatic molecular dynamics simulations, revealed that Ta reduction induced by  $v_N$  is a key factor in reducing the carrier lifetime of  $Ta_3N_5$  photoanodes [21, 32–34]. They also demonstrated that Mg doping can modulate the charge distribution of Ta species near  $v_N$ . However, dopants with larger ionic radii can introduce residual strain, potentially affecting crystalline and introducing charge-trapping states at grain boundaries. For example,  $La^{3+}$  (103 pm),  $Mg^{2+}$  (72 pm), and  $Zr^{4+}$  (72 pm) have significantly larger ionic radii compared to  $Ta^{5+}$  (64 pm), meaning that excessive doping can lead to substantial structural alterations [14, 17, 30]. Though, recently Fan et al. [15] performed hybrid DFT calculations as predicted Ti as a promising dopant for  $Ta_3N_5$  has been proposed. Their findings indicate that increasing Ti doping concentrations shifts both the valence and CB edges of  $Ta_3N_5$  toward more negative potentials, which contrasts with the role of oxygen impurities also  $Ti^{4+}$  has an ionic radius 61 pm which is quite near to  $Ta^{5+}$ .  $Ta_3N_5$  crystallizes in an orthorhombic structure (SG:  $Cmcm$ ), with two nonequivalent Ta and three distinct N sites. Thus, by carefully controlling the levels of O and Ti doping, the band-edge positions can be optimized to enhance the PEC performance [15]. Also, the formation of point defects alters both local and overall electronic structures with in-gap defects significantly affecting charge transport and photocarrier recombination, affecting PEC efficiency. Thus, the charge compensation through precise doping at controlled concentrations offers a promising strategy to mitigate intrinsic in-gap states and reduce exciton recombination rates [13].

In this regard, Ti emerges as promising dopant due to its similar ionic radii to Ta and ability to suppress  $O_N$  incorporation, leading to lower onset potentials. While Ti doping has been shown to enhance PEC performance, its exact role in modifying local and electronic structure remains unclear. Furthermore, the unconventional two-step process oxidation followed by nitridation of Ta foils results in high oxygen content (>10 at%) in  $Ta_3N_5$  films, complicating evaluation of compensation effects. So far, the understanding the nature of these defects and influence of doping, particularly with Ti, is largely limited to theoretical calculations [13, 15]; and only limited experimental reports are available [34]. A systematic experimental characterization of point defects and understanding of doping are lacking.

In this study, we employ a highly controllable single-step reactive magnetron co-sputtering deposition process to synthesize Ti-doped  $Ta_3N_5$  thin films. The ultrahigh vacuum (UHV) conditions

minimize impurity incorporation from residual gases. This approach allows for precise control over layer composition, thickness, and crystallinity [35–37]; facilitating a systematic investigation of Ti incorporation effects on structural and optical properties. We utilize synchrotron-based bulk sensitive hard X-ray photoelectron spectroscopy (HAXPES) and X-ray absorption near edge spectroscopy (XANES) measurements complimented by the theoretical simulations to understand the role of site-specific substitution of Ti on defect states. By elucidating the impact of Ti doping on defect states and charge transport, this study aims to provide critical insights into optimizing  $Ta_3N_5$  photoanodes for efficient solar water splitting.

## 2 | Experimental and Computational Details

### 2.1 | Thin Film Growth

Ti-doped  $Ta_3N_5$  films were deposited on  $1 \times 1 \text{ cm}^2$  *n*-type Si(111), Ta, fused silica ( $SiO_2$ ) substrates using reactive direct current magnetron co-sputtering of elemental 75 mm Ta (99.99% purity) and 50-mm Ti (99.99% purity) targets. Si has resistivity 1–6  $\Omega \text{ cm}$  and Ta substrates have sheet resistance of 2–5 ohm/sq. The target to substrate distance is 12 cm. Prior to deposition, all substrates were cleaned using Hellmanex III solution, acetone, and isopropanol for 15 min each, followed by drying in  $N_2$  gas flow. During the sputtering, a gas mixture of Ar,  $N_2$ , and  $O_2$  were used with the gas-flow ratio of 2:3:0.2. Ti doping was done by co-sputtering Ti and Ta where the Ti concentration was controlled by varying the Ti magnetron power from 0 to 100 W while keeping the Ta power fixed to 300 W. The deposition chamber was evacuated to the base pressure of  $2.6 \times 10^{-6} \text{ Pa}$  ( $2 \times 10^{-8} \text{ Torr}$ ) before the deposition while during the film growth the pressure was 0.67 Pa (5 mTorr) due to the flow of process gases. The substrates were rotated at 30 rpm for better uniformity. Initially the 10 nm seed layer of  $TaO_x$  thin film was deposited at ambient temperature, and then substrate temperature was raised to 1000°C for the final film deposition. The approx. thickness of the grown films was in between 550 and 600 nm. More details and growth parameters can be found elsewhere [35–37].

### 2.2 | Thin Film Characterization

The crystal structure of samples was analyzed by  $\theta/2\theta$  X-ray diffraction (XRD) using a PANalytical Bragg–Brentano diffractometer with a Cu- $K\alpha$ ,  $\lambda = 1.5406 \text{ \AA}$  source. The composition of the films was measured by a combination of Rutherford backscattering spectrometry (RBS) and time-of-flight elastic recoil detection analysis (ToF-ERDA) [38]. 2 MeV  $He^+$  primary ion beam was incident at 5° to the sample normal, and the backscattered particles were detected at an angle of 170°. For ToF-ERDA measurements, a 36 MeV iodine ( $^{127}I^{8+}$ ) primary beam was incident at an angle of 67.5° with respect to the sample surface normal. The light element composition was extracted from elemental depth profile using *Potku* code [39]. The morphology of films was characterized using a field-emission gun scanning electron microscope (SEM), LEO 1550 Gemini. To investigate the local and electronic structure, XANES measurements were performed at room temperature (RT) in florescence mode at BL-09 beamline,

at the Indus-2 synchrotron radiation source at RRCAT, Indore, India. The background removal of the XANES spectra was done using ATHENA software [40]. HAXPES measurements were performed at the P22 beamline of the PETRA III synchrotron radiation source (Hamburg, Germany) using incident photon energy of 6 keV measured at RT. A hemispherical energy analyzer (SPECS Phoibos 225 HV) was employed, with an overall energy resolution of approximately 150 meV [41]. The steady-state photoluminescence (PL) spectra are measured using FLS 1000 EDINBURG INSTRUMENTS PL spectrometer under excitation of a 473 nm laser measured at RT. The time-resolved PL was acquired with 375 nm picosecond laser pulsed at a repetition rate of 10 MHz as an excitation source with the emission was collected at 580 nm measured at RT. The absorbance was measured using an Agilent Cary series ultraviolet–visible (UV–vis) spectrophotometer. The UV–vis spectra were measured on films grown on fused silica substrates, and PEC measurements were performed on the films grown on Ta substrates, while the remaining characterizations were carried out on films grown on Si (111) substrates.

### 2.3 | Photoelectrocatalysis Characterization

PEC experiments were run in a 150 mL quartz tube filled with 120 mL of 1 M  $NaOH$  + 0.1 M  $K_4Fe(CN)_6$  solution (measured pH = 12.8). The cell was configured in a three-electrode configuration, with the Ti-doped  $Ta_3N_5$  photoanode as the working electrode,  $Ag/AgCl/3M KCl$  as the reference electrode, and a Pt mesh as counter electrode. All the measured potentials were converted to RHE scale by using the Nernst equation:

$$V_{RHE} = V_{Ag/AgCl} + V_{Ag/AgCl}^0 + 0.059 * pH$$

where  $V_{Ag/AgCl}^0 = 0.200V$  is the standard redox potential of the  $Ag/AgCl$  couple against SHE scales. Electrochemical measurements were carried out through a Gamry Interface 1000 potentiostat, while illumination was provided by a Quantum Design solar simulator, LS 0306, with a 300 W Xe lamp coupled with an AM 1.5 G filter. The total light irradiance was 100 mW/cm<sup>2</sup> on a 4 cm circular spot. For each electrode, at the beginning, a cyclic voltammetry (CV) was run at 50 mV/s with 10 mV step to clean the surface and stabilize the system. Linear sweep voltammetry, LSV, was run at 10 mV/s and 5 mV, while light was automatically chopped every 2 s through a homemade chopper. Open circuit potentials, OCPs, were run after stabilization ( $V_{drift} < 0.5 \text{ mV/s}$ ), by switching from dark to light every 2 min. Finally, electrochemical impedance spectroscopy, EIS, was run from 0.55 to 1.2 V versus RHE, from 20 kHz to 0.1 Hz with a 10 mV rms AC perturbation.

### 2.4 | Computational Details

First-principles calculations were performed by means of DFT and the projector augmented wave method (PAW) [42]; as implemented in the Vienna ab-initio simulation package (VASP) [43]; accounting for the effect of spin–orbit interaction. The calculations were made both with unit cells containing 6 Ta and 10 N atoms as well as in supercells with a plane-wave expansion cutoff

energy set to 400 eV. The calculations were made using a  $1 \times 1$  primitive unit cell  $\text{Ta}_3\text{N}_5$  structure with  $a_p = b_p = 5.521 \text{ \AA}$  and  $c_p = 10.357 \text{ \AA}$ . The on-site Coulomb correction (GGA + U) [44]; for Ta was calculated as  $U = 3.5$  [45], reflecting the screened atomic correlation energy [46]. A  $2 \times 2$  supercell containing 12 Ta and 20 N atoms was needed to include Ti substitution on the different sites. XAS were calculated using a full width at half maximum core-hole lifetime set to 0.8 eV at the Ti 1s-edge.

### 3 | Results and Discussion

#### 3.1 | Effect of Ti Doping on Structure and Composition of $\text{Ta}_3\text{N}_5$ Films

Figure 1a shows  $\theta/2\theta$  XRD patterns acquired from the as-deposited thin films on Si(111) with varying Ti power together with a simulated reference pattern of  $\text{Ta}_3\text{N}_5$ . Regardless of the Ti power, all diffraction peaks closely align with the reference pattern indicating that all films retain orthorhombic crystal structure (space group:  $Cmcm$ ) and implying that Ti incorporation does not alter the overall crystal structure of  $\text{Ta}_3\text{N}_5$ . Although the XRD patterns appear similar across all Ti-doped samples, a systematic shift in diffraction peaks toward higher  $2\theta$  values can be seen as indicated by vertical drop lines. This shift results from the lattice contraction with increasing Ti power. The calculated lattice

parameters ( $a$ ,  $b$ , and  $c$ ) as a function of Ti power are presented in Figure 1b. There is a decreasing trend in all three lattice parameters as the Ti power increases. Given that the ionic radius of  $\text{Ti}^{4+}$  (60.5 pm) is slightly smaller than that of pentavalent  $\text{Ta}^{5+}$  (64 pm), this reduction in lattice parameters hints the substitution of Ta atoms by Ti within the  $\text{Ta}_3\text{N}_5$  matrix rather than interstitial occupation or the formation of secondary phases [15].

To assess the bulk composition of the as-deposited films, RBS and ERDA were conducted. The representative curves are shown in Figure S1, and the obtained film composition is summarized in Table S1. The concentrations of Ta, Ti, N, and O as functions of Ti sputtering power are plotted in Figure 1c. The results indicate a linear increase in Ti content with increasing Ti sputtering power, ranging from 0 at% at 0 W to a maximum of 10 at% at the highest power setting of 100 W. Concurrently, the Ta content successively decreases. Thus, the contraction of unit-cell parameters along with composition supporting the notion that Ti atoms are substituting for Ta atoms in the  $\text{Ta}_3\text{N}_5$  structure. In addition to the variations in Ti and Ta content, a noticeable increase in O concentration is observed with increasing Ti doping. Specifically, the O content rises from approximately 1.5 at% in undoped  $\text{Ta}_3\text{N}_5$  films to about 6 at% at the highest Ti doping levels (see Figure 1c). A similar trend of increased oxygen content upon Zr doping has been reported, which contrasts with recent findings on Ti-doped  $\text{Ta}_3\text{N}_5$  films, where oxygen content decreased with Ti incorporation [34]. One possible reason for the notable increase in

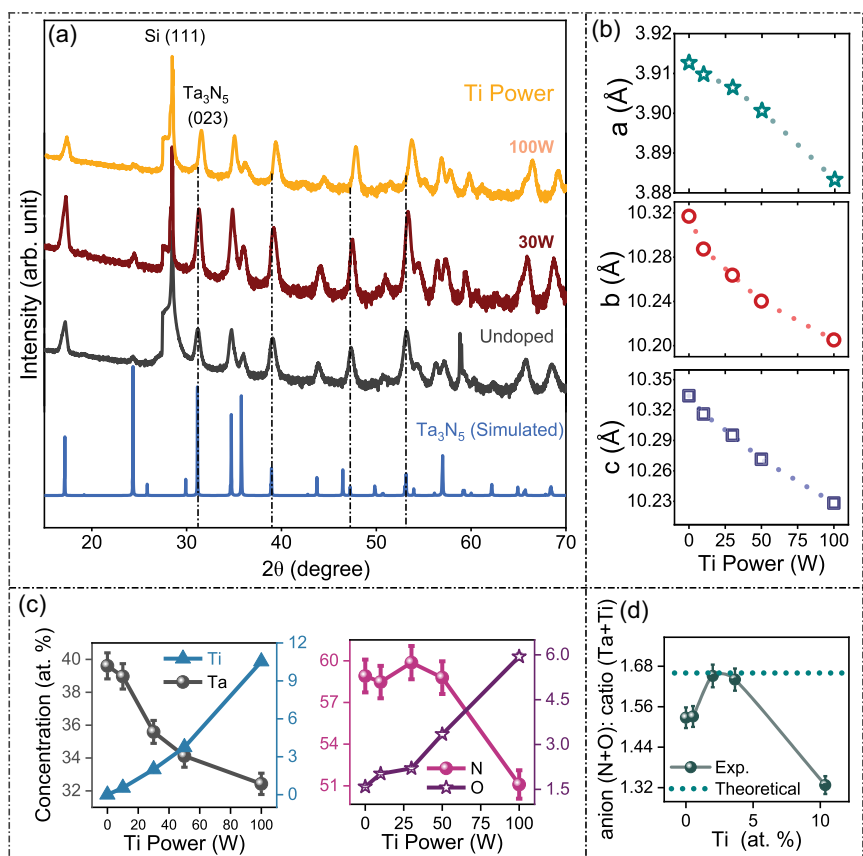


**FIGURE 1** | (a) X-ray diffraction (XRD) patterns of undoped, Ti-doped (30 and 100 W)  $\text{Ta}_3\text{N}_5$  thin films, compared with simulated XRD patterns of orthorhombic  $\text{Ta}_3\text{N}_5$ . Vertical drop lines are included to enhance the visibility of peak shifts. (b) Lattice parameters as a function of Ti doping. (c) Atomic concentrations of Ta, Ti and N, O plotted with respect to Ti sputtering power. (d) Anion (N + O) to cation (Ta+Ti) ratio plotted as a function of Ti atomic concentration. A guideline is included to show the trend across the data points.

oxygen content with Ti doping concentration in the present study could be the difference in growth methods compared to earlier reports. As Wagner et al. [34] deposited Ti-doped  $\text{TaO}_x$  films and then converted  $\text{Ta}_3\text{N}_5$  via  $\text{NH}_3$  annealing. Another factor could be the higher affinity or solubility of Ti for oxygen compared to Ta, which may promote enhanced oxygen incorporation during film growth in the current samples.

Apart from Ti and O, the N content plays a crucial role in determining the electrical and optoelectronic properties of  $\text{Ta}_3\text{N}_5$  films, as  $\text{v}_N$  are known to act as deep donors that contribute to charge recombination [12, 20, 22, 35]. The measured N concentration initially shows a slight increase from 58.1 to around 60 at% as Ti sputtering power increases from 0 to 30 W (see Figure 1c). It indicates that the undoped  $\text{Ta}_3\text{N}_5$  has a slight N deficiency, which decreases after Ti doping (2 at%). However, beyond this Ti doping level, N content begins to reduce significantly. This suggests that moderate Ti doping may help mitigate N deficiency in  $\text{Ta}_3\text{N}_5$  films, but excessive Ti incorporation above 3.5 at% eventually leads to N reduction, possibly due to changes in the growth kinetics or enhanced O uptake. Further, the ratio of anion (N + O) to cation (Ta + Ti) elements as a function of Ti concentration is plotted in Figure 1d. This ratio is compared with the ideal stoichiometric ratio for  $\text{Ta}_3\text{N}_5$  (1.66). It reveals a dome-like trend, where the anion to cation ratio initially increases with Ti doping, reaching an optimal value within the Ti concentration range of 2.0–3.5 at%. Beyond this range, the ratio decreases again, indicating deviations from  $\text{Ta}_3\text{N}_5$  composition at higher Ti doping levels. This behavior suggests that low to moderate Ti doping may improve film stoichiometry by compensating for intrinsic  $\text{v}_N$ , but excessive doping disrupts the balance, leading to increased O incorporation and N reduction.

A recent study by Wagner et al. [34] reported that the XRD patterns of Ti-doped (up to the 3.5 at%)  $\text{Ta}_3\text{N}_5$  thin films deposited using two-step growth method on n-type Si substrates. They showed films remain unaltered, suggesting no significant changes in the lattice parameters after doping. Additionally, they observed a decrease in bulk oxygen content with increasing Ti concentration, which contrasts with the present findings which could be due to difference in growth methods. However, despite the small mismatch in ionic radii of Ti and Ta, the introduction of Ti can still induce lattice strain and impact the crystallite size (CS) of the films. To evaluate this effect the lattice strain was estimated using relative change in the  $a$ ,  $b$ ,  $c$  lattice parameters, and CS was estimated using the Scherrer equation [47] from the (023) reflection as marked in Figure 1a and calculated CS are given in Table S1 of SM. It indicates that at low Ti doping levels (up to 2 at%), the CS remains relatively at approximately 41–43 nm, with minimal strain (−0.01%). However, at higher doping levels (3.5 at%), a noticeable reduction in CS is observed (31–33 nm). This decrease is accompanied by a small compressive strain (−0.05%), which suggests that excessive Ti doping can introduce lattice distortions and defect formations. The reduction in CS at higher Ti concentrations may negatively impact the charge transport properties of the films, as smaller grain can introduce more grain boundaries, which act as recombination centers for charge carriers [48]. Overall, the structural compatibility between Ti and Ta due to their similar ionic sizes suggests that substitutional incorporation of Ti at Ta sites is feasible up to a doping concentration of approximately 2 at%. At this optimal doping level,

Ti might compensate the excess donor states created by  $\text{v}_N$  or  $\text{O}_N$  defects without significantly modifying the crystal structure. Representative surface morphologies of the undoped and 2 at% Ti-doped thin films are shown in Figure S2, demonstrating that the plate-like morphology is retained after Ti doping. Cross-sectional SEM images reveal column-like structures, which are often visible in dcMS-grown films [49, 50]. The thickness of the undoped  $\text{Ta}_3\text{N}_5$  film is ≈560 nm, increasing to around 580 nm upon Ti incorporation. To further investigate synergistic effect, a detailed analysis of the electronic structure of these films is presented in the following section.

### 3.2 | Electronic Structure Studies Using HAXPES and XANES

To investigate the influence of Ti doping on the electronic structure  $\text{Ta}_3\text{N}_5$ , bulk-sensitive HAXPES measurements were conducted. With a probing depth of approximately 15–20 nm at 6 keV, this technique does not require surface cleaning treatment or Ar etching, making it well-suited for analyzing the bulk chemical and electronic structure. Figure 2a,b present normalized HAXPES spectra of the Ta 4f and N 1s core-levels for undoped, 2, and 3.5 at% Ti-doped  $\text{Ta}_3\text{N}_5$  thin films, respectively. In Ta 4f core-levels, the primary peaks observed at approximately 25.6 and 27.5 eV correspond to the spin-orbit split  $\text{Ta} 4f_{7/2}$  and  $4f_{5/2}$  core-levels, which are characteristic of the  $\text{Ta}_3\text{N}_5$  phase. In the case of the undoped  $\text{Ta}_3\text{N}_5$  sample, both peaks exhibit a noticeable asymmetry toward the lower binding energy region, which is typically indicative of the presence of sub-stoichiometric Ta species, such as  $\text{Ta}^{(5-\delta)+}$ . Very often such lower asymmetry is assigned to the  $\text{Ta}^{3+}$  charge-state [14, 17, 20, 51]. Interestingly, this asymmetry reduces with Ti doping to 2 at% but becomes more pronounced again at 3.5 at% Ti doping. This trend suggests that Ti incorporation at lower concentrations may stabilize the electronic structure of  $\text{Ta}_3\text{N}_5$  by reducing the presence of lower-valence Ta species. However, at higher Ti doping levels, structural distortions or oxygen incorporation may again lead to the re-emergence of these lower energy features. Similarly, the N 1s peak intensity exhibits an enhancement at 2 at% Ti doping compared to the undoped  $\text{Ta}_3\text{N}_5$  sample but subsequently decreases at 3.5 at% Ti doping (see inset of Figure 2b). This observation suggests that N concentration in films improves at the optimum Ti doping level of 2 at%.

To gain more insight into the chemical states present in the films, the Ta 4f peaks were deconvoluted into three distinct doublets ( $\text{Ta} 4f_{7/2}$ – $\text{Ta} 4f_{5/2}$ ) using a fixed area ratio of 4:3 and a spin-orbit splitting of 1.9 eV (see Figure S3). The binding energies of the  $\text{Ta} 4f_{7/2}$  components were identified at 24.8, 25.6, and 26.2 eV, corresponding to reduced Ta species ( $\text{Ta}^{(5-\delta)+}$ ), stoichiometric  $\text{Ta}_3\text{N}_5$  ( $\text{Ta}^{5+}$ ), and oxygen-substituted  $\text{Ta}_3\text{N}_5$  ( $\text{TaON}$ ), respectively. Quantitative analysis of these species is provided in Table S2. In the undoped  $\text{Ta}_3\text{N}_5$  thin film, the estimated relative at% composition of Ta in the form of  $\text{Ta}^{(5-\delta)+}$ ,  $\text{Ta}_3\text{N}_5$ , and  $\text{TaON}$  is approximately 26.6%, 58.4%, 15.0%, respectively. Notably, after doping with 2 at% Ti, the fraction of  $\text{Ta}_3\text{N}_5$  increases to 84.3%, while the reduced  $\text{Ta}^{(5-\delta)+}$  species are drastically suppressed to 3.7%. Meanwhile, the  $\text{TaON}$  component exhibits only a slight change to 12%. This result strongly suggests that Ti doping at 2 at% helps to suppress the formation of reduced Ta species and

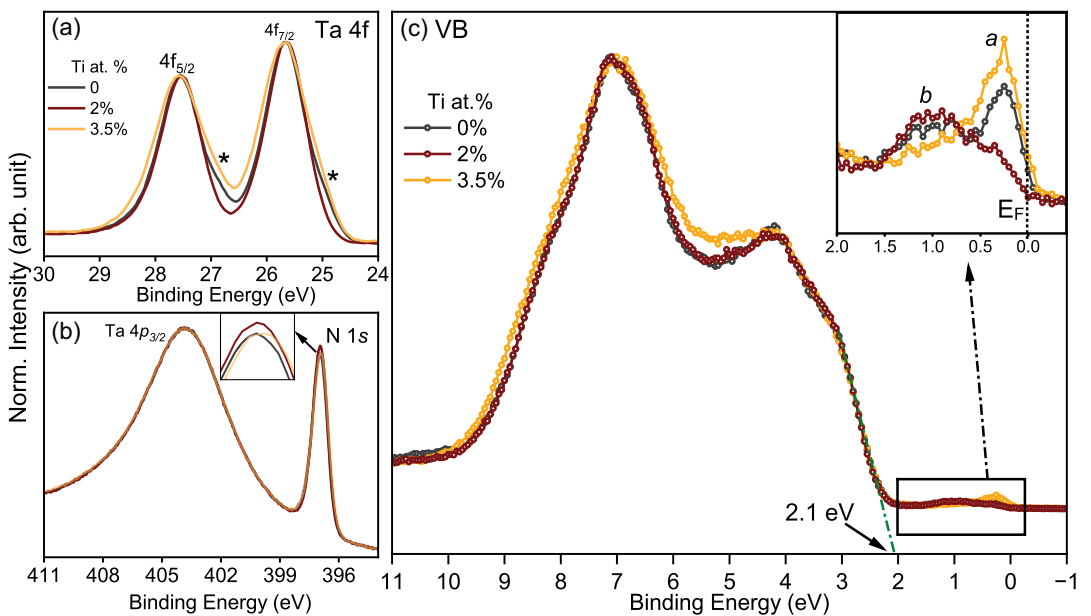


**FIGURE 2** | (a) Ta 4f, (b) N 1s core-level hard X-ray photoelectron spectra with an inset shows zoomed view of undoped, 2 and 3.5 at% Ti-doped  $\text{Ta}_3\text{N}_5$  thin films. (c) Valence band spectra measured using hard X-rays of undoped, 2 and 3.5 at% Ti-doped  $\text{Ta}_3\text{N}_5$  thin films. Inset shows zoomed view near Fermi-Level.

stabilizes the near stoichiometric  $\text{Ta}_3\text{N}_5$  phase. However, at a higher doping concentration of 3.5 at%, the composition shifts once again, with  $\text{Ta}_3\text{N}_5$  decreasing to 59.4%, while  $\text{TaON}$  and  $\text{Ta}^{(5-8)+}$  species increase to 22.2% and 18.4%, respectively. Thus, excessive Ti doping may lead to incorporate more  $\text{O}_N$  or structural distortions that reintroduce reduced tantalum species. To further understand the electronic structure, the valence band (VB) of these samples was probed using HAXPES, as shown in Figure 2c. The band edge position of undoped  $\text{Ta}_3\text{N}_5$  is located approximately 2.1 eV below the Fermi-level ( $E_F$ ), remaining unchanged with 2 and 3.5 at% Ti doping without creating new acceptor states. Additionally, the overall shape of the VB for the 2 at% Ti-doped sample closely resembles that of undoped  $\text{Ta}_3\text{N}_5$ , indicating minimal changes in the VB structure. However, at higher Ti doping (3.5 at%), noticeable modifications occur, with new states emerging around 5 eV. A particularly important observation is the presence of distinct in-gap defect states near the  $E_F$ , as shown in the inset of Figure 2c. In undoped  $\text{Ta}_3\text{N}_5$ , two distinct defect states appear at  $\approx 0.22$  and  $0.93$  eV (assigned as feature *a* and *b*, respectively) below  $E_F$ . Recent DFT calculations attributed similar defect features to  $\text{v}_N/\text{Ta}^{3+}$  and  $\text{O}_N$  states [20].  $\text{O}_N$  is predicted to generate shallow donor levels just below the CB, whereas the  $\text{v}_N$  and reduced Ta defects form deep trap states below the CB, respectively. Furthermore, with optimal Ti doping (2 at%), feature *a* is significantly suppressed, while feature *b* shows a slight enhancement. However, the overall area under the curve of these defect states is significantly reduced after optimum doping, suggesting that a Ti incorporation of  $\approx 2$  at% effectively mitigates some of these deep trap states.

Furthermore, due to weaker signal at lower doping and overlapping Ti 2p and Ta 4p<sub>1/2</sub> core-level, it is difficult to do any qualitative assessment using HAXPES (see Figure S4). Thus, to understand the electronic structure and confirm the isostructural incorporation of Ti into the  $\text{Ta}_3\text{N}_5$ , element sensitive

XANES measurements were performed. XANES is highly sensitive to both the local electronic structure and coordination environment of the absorbing atom, making it an invaluable tool for investigating the incorporation of Ti into  $\text{Ta}_3\text{N}_5$ . Figure 3a presents the Ti *K*-edge XANES spectra for 0.5, 2, and 3.5 at% Ti-doped samples, along with reference spectra for Ti,  $\text{TiN}$ , and  $\text{TiO}_2$ . Herein, the *K*-edge corresponds to the electronic transition from the Ti 1s core-level to unoccupied 4p orbitals, allowed by the dipole selection rule ( $\Delta l = \pm 1$ ). A key feature of XANES spectroscopy is that an increase in the valence state of the absorbing ion leads to a systematic shift of the absorption edge to higher energies [52]. Additionally, for a given oxidation state, the edge position is further influenced by the electronegativity of the coordinating anions, higher electronegativity results in a higher energy shift. In the case of Ti incorporation into  $\text{Ta}_3\text{N}_5$ , Ti ions are expected to achieve a maximum oxidation state of  $\text{Ti}^{4+}$  and be coordinated primarily with nitrogen atoms. Based on trends shown in the reference spectra, the Ti species incorporated within the  $\text{Ta}_3\text{N}_5$  matrix should exhibit an absorption edge that falls between those of  $\text{TiN}$  and  $\text{TiO}_2$ . Thus, the absorption edge positions of Ti-doped samples are observed between those of  $\text{TiN}$  and  $\text{TiO}_2$ , strongly indicating that Ti is present in a tetravalent oxidation state ( $\text{Ti}^{4+}$ ) and is iso-structurally incorporated into the  $\text{Ta}_3\text{N}_5$  lattice. It can be further evidence in Figure 3a, where the covalency is plotted as a function of edge energy. Additionally, the spectral features show no obvious contribution from metallic Ti or  $\text{TiN}$  like states, which would be expected to appear at lower photon energies. This effectively rules out the possibility of  $\text{TiN}$  phase formation in the doped films, at least up to 3.5 at% Ti doping. Instead, the results suggest that Ti primarily substitutes Ta atoms in the  $\text{Ta}_3\text{N}_5$  lattice while remaining coordinated with N and O atoms in the first coordination shell.

Figure 3b,c shows two illustrations of the orthorhombic  $\text{Ta}_3\text{N}_5$  crystal structure. Here, Ta occupies two nonequivalent crystallographic sites which are coordinated with three or

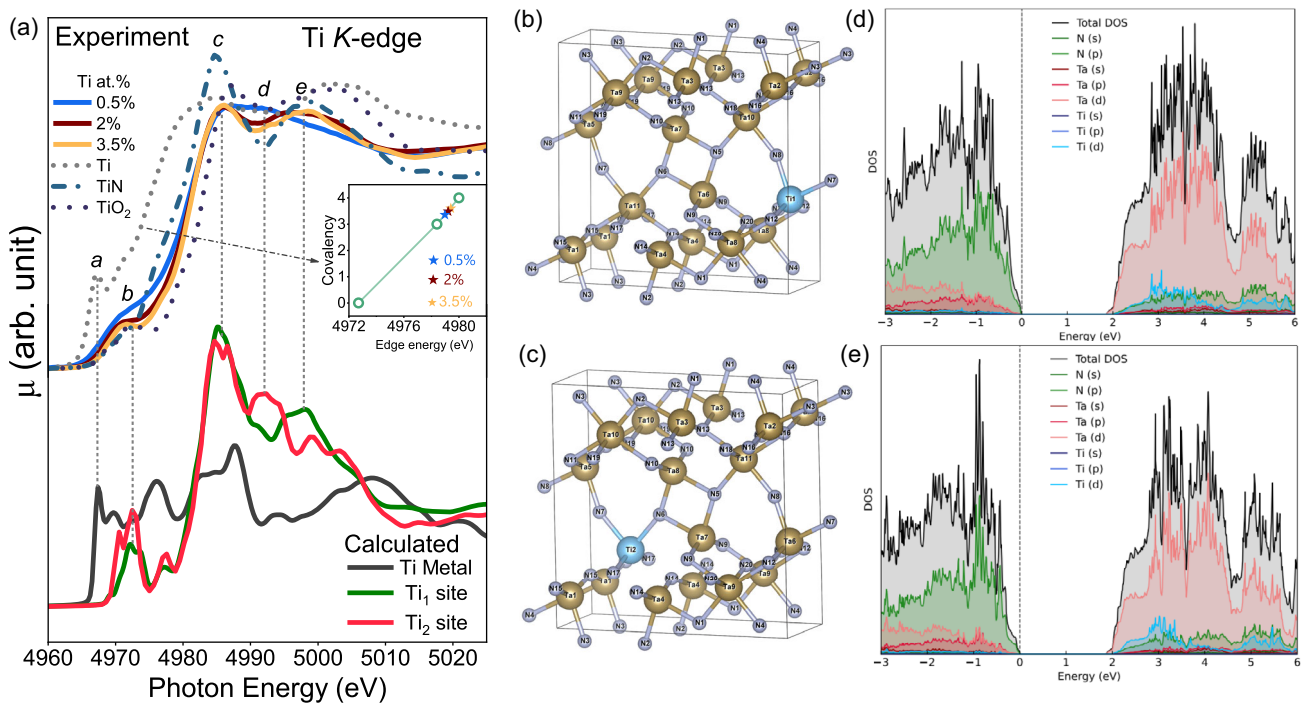


**FIGURE 3** | (a) Simulated Ti K-edge X-ray absorption near edge spectra compared with experimental once obtained for 0.5, 2, and 3.5 at% Ti-doped samples and Ti, TiN, TiO<sub>2</sub> references, with an inset depicting covalency as a function of absorption edge energy, derived from the first derivative of the spectra. DFT-GGA optimized crystal structures of Ta<sub>3</sub>N<sub>5</sub> with Ti substituted at different sites of Ta, namely, (b) Ti<sub>1</sub> and (c) Ti<sub>2</sub>. Density of states plots of 3.1 at% Ti-doped (d) Ti<sub>1</sub> and (e) Ti<sub>2</sub> sites in Ta<sub>3</sub>N<sub>5</sub>.

four-coordinated N atoms. Thus, to investigate the site-specific substitution behavior of Ti in this structure, we performed simulations of Ti K-edge XANES spectra. First, we obtained relaxed atomic structures of Ta<sub>3</sub>N<sub>5</sub> with Ti substituting at the two distinct Ta sites: Ti<sub>1</sub>, substituting Ta atom coordinated by three nitrogen atoms; and Ti<sub>2</sub>, substituting Ta atom coordinated by four nitrogen atoms. The theoretical XANES spectra were calculated using VASP6 based on these relaxed structures. The relaxed structures are given in Figures 3b,c for Ti<sub>1</sub> and Ti<sub>2</sub> sites substitutions, respectively. The simulated spectra show excellent agreement with the experimental Ti K-edge XANES data, reproducing all major spectral features marked as *a*, *b*, *c*, *d*, and *e* (see Figure 3a). Simulated spectra were aligned to experimental once using reference Ti spectra where an intense pre-feature *a* can be seen. At low Ti doping concentration (0.5 at%), distinct features labeled as *b*, *c*, and *d* are observed in the experimental spectrum. Notably, these features are only replicated in the simulated spectrum for Ti<sub>2</sub> substitution, suggesting that Ti preferentially occupies the four-fold N-coordinated Ta sites at low doping level. However, at higher Ti concentrations, feature *d* disappears, and a new feature *e* emerges in the experimental spectrum alongside with reduction in pre-feature *a* intensity, these observations are again reproduced exclusively in the simulation for the Ti<sub>1</sub> site, where Ti replaces the three-fold coordinated Ta. From these results, it can be concluded that the site preference of Ti in the Ta<sub>3</sub>N<sub>5</sub> lattice is doping/concentration dependent. At lower Ti concentrations, Ti substitution is structurally favorable at the Ta site (Ti<sub>2</sub>) bonded with four coordinated N. While at higher concentrations, Ti preferentially occupies the Ta site (Ti<sub>1</sub>) which is coordinated with three N atoms. This site-dependent substitution behavior plays a critical role in determining the local structure and electronic environment of Ti in Ta<sub>3</sub>N<sub>5</sub>, as revealed by

the XANES simulations. The computed density of states (DOS) for both these Ti-doped Ta<sub>3</sub>N<sub>5</sub> structures at Ti<sub>1</sub> and Ti<sub>2</sub> site are shown in Figures 3d,e, respectively. Herein, the VB (below E<sub>F</sub>) is dominated by N 2p states hybridized with Ta 5d and Ta 5p states with some contribution of Ta 6s states and Ti 3d states. While the CB is dominated by Ta 5d, Ti 3d hybridized with N 2p with smaller contributions of Ta 5p, 5s, N 2s, and Ti 4s, 4p orbitals. Interestingly, it can be seen for both Ti sites; there are no new states that appear within the band gap while a strong contribution from Ti 3d states analogous to Ta 5d states can be seen in the CB. However, the observed Ti 3d states near CB can narrow a bandgap slightly of Ta<sub>3</sub>N<sub>5</sub> alongside as compared to Ti<sub>1</sub>, Ti<sub>2</sub> site, which shows strong contribution near CB minima can be seen. It is worth mentioning here that Ti substitution alone cannot create new in-gap defect states [13, 15]. However, to reproduce the exact in-gap defect states observed in the VBS shown in Figure 2c detailed DFT calculations on more complex super-structures are required.

### 3.3 | Optical Properties of Ti-Doped Ta<sub>3</sub>N<sub>5</sub> films

Figure S5 presents the UV-Vis absorption spectra for Ta<sub>3</sub>N<sub>5</sub> films with varying concentrations of Ti doping (0–10 at%). The observed absorption onset corresponds to electronic transitions from the N/O 2p orbitals, which predominantly constitute the VB to the Ta 5d orbitals forming the CB [12]. With increasing Ti doping, a redshift in the absorption edge is evident reduction of the optical bandgap at least at higher doping of Ti (>3.5 at%).

Furthermore, Figures 4a,b present the room-temperature measured steady-state and time-resolved PL emission spectra

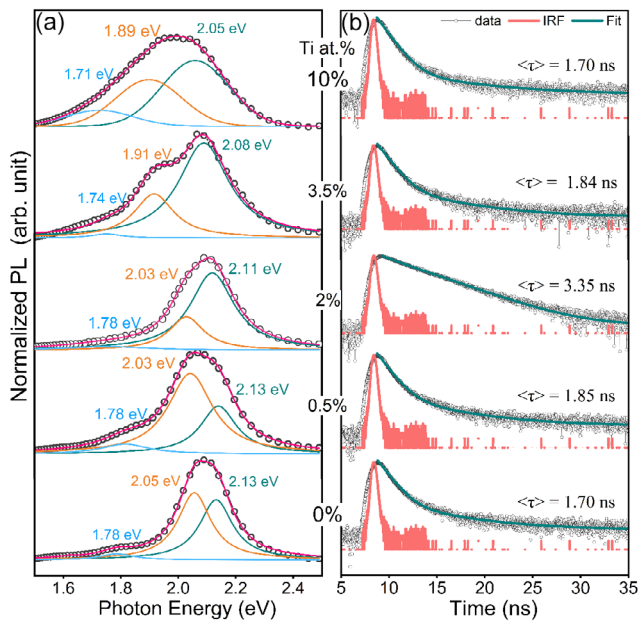


**FIGURE 4** | (a) Fitted steady state and (b) time resolved photoluminescence (TRPL) along with instrumental resolution function of Ti-doped  $\text{Ta}_3\text{N}_5$  thin films measured at room temperature. Steady-state PL spectra were fitted using the Lorentz function and TRPL spectra were fitted using double exponential decay function and the fitting parameters of TRPL are given in table S3, Supporting Information.

of  $\text{Ta}_3\text{N}_5$  thin films with different Ti doping. In the steady-state PL, as the Ti concentration increases, the spectra broaden and exhibit a redshift, signifying a progressive narrowing of the optical band gap or presence of multiple emission processes (see Figure 4a). To gain deeper insights, we fitted the PL spectra using a Lorentzian shape profile. For the undoped  $\text{Ta}_3\text{N}_5$  sample, the absorption band at approximately 2.13 eV corresponds to the intrinsic band edge emission of  $\text{Ta}_3\text{N}_5$ , while the broad peak near 2.05 eV is very often associated with  $\text{O}_N$  defects, introducing shallow donor levels below the CB. Additionally, a deep-level emission at 1.78 eV is observed, which might be attributed to radiative recombination by  $\text{v}_N$  or reduced Ta ( $\text{Ta}^{(5-\delta)+}$ ) [20]. These obtained defects agree with the in-gap defect states visualized in VBS. However, it is not possible to distinguish the contribution of these two types  $\text{v}_N$  or reduced Ta ( $\text{Ta}^{(5-\delta)+}$ ) defects solely based on room-temperature PL data and required the low-temperature PL measurements [20]. However, the observations of these in-gap emissions corroborate with RBS and HAXPES results showing that undoped  $\text{Ta}_3\text{N}_5$  sample has 1.5 at% O and slightly lower N concentration, which can produce reduced Ta states. With 0.5 at% Ti doping, the PL spectra are primarily dominated by  $\text{O}_N$  and  $\text{v}_N/\text{Ta}^{(5-\delta)+}$  defect-related emissions since Ti has more affinity towards O as compared to Ta thus as  $\text{Ti}_{\text{Ta}}$  substitution incorporated more  $\text{O}_N$ , thus the intensity of defect band at 2.03 eV is enhanced (see Figure 4a). Interestingly, 2 at% Ti doping, the near-band-edge emission is significantly enhanced, whereas defect emissions are suppressed. However, at 3.5 at% Ti doping, both the band-edge emission and defect-related emissions continue to strengthen, with their intensities progressively rising to 10 at% Ti. Also, PL spectra exhibit redshift in emission at Ti doping levels  $\geq 3.5$  at%, consistent with the absorption spectra and DOS calculations. This bandgap narrowing is attributed to

the incorporation and hybridization of Ti 3d states within the CB, which alter the electronic structure of  $\text{Ta}_3\text{N}_5$ . Thus, PL results suggest that at an optimum Ti doping concentration of 2 at%, defect-related emissions are suppressed. These results are in good agreement with the theoretically predictions which show that the controlled Ti-O co-doped  $\text{Ta}_3\text{N}_5$ , Ti doping can compensate for the effect of O impurities as well as reduce the  $\text{Ta}^{3+}$  charge states by creating charge compensation effect [15].

To gain further insight into the effect of Ti doping on carrier dynamics, time-resolved PL measurements were conducted, as plotted in Figure 4b. Herein, the prolonged lifetime can be directly visualized for the optimum Ti-doped  $\text{Ta}_3\text{N}_5$  thin films. To get further details, the decay curves were fitted using the biexponential decay model, and the fitting parameters are listed in Table S3 of the SM. The fast component lifetime ( $\tau_1$ ) is ascribed to the defect-related trapping of the photogenerated carriers while the slow component ( $\tau_2$ ) originates from the electron–hole recombination from conduction to valence band [17]. The extracted values reveal a significant variation in carrier lifetime across different doping levels. The PL decay of the undoped  $\text{Ta}_3\text{N}_5$  is dominated (83.28%) by the  $\tau_1$  suggesting the dominance of defects related recombination with a lifetime of 0.99 ns and average  $\langle\tau\rangle$  of 1.70 ns. With the small doping of Ti (0.5 at%) it is slightly increased, and for optimum doping the fractional intensity of the fast component ( $f_1$ ) reduces drastically to only 1.76%. Furthermore, at higher doping of 3.5 at% dominance of fast decay component can be seen. The longest exciton lifetime is observed at an optimum doping level of 2 at%, which coincides with the suppression of in-gap defect bands in the steady-state PL spectra and HAXPS results. It is well-documented that such defect states serve as charge carrier recombination centers, leading to increased nonradiative recombination and reduced carrier lifetimes [17, 33, 51]. The shorter exciton lifetime observed in the undoped  $\text{Ta}_3\text{N}_5$  sample further corroborates the presence of a higher density of point defects, which facilitate rapid carrier recombination. The significant reduction in the fast decay component at 2 at% Ti doping strongly suggests that defect states are effectively passivated at this concentration, thereby reducing nonradiative recombination pathways. The reduction in exciton lifetime at 3.5 at% Ti doping indicates an increase in nonradiative recombination processes, likely due to the reintroduction of defect states, increase in O content thus increased carrier trapping at high Ti concentrations. This suggests that excessive Ti incorporation may lead to unintended defect formation, thereby counteracting the beneficial effects observed at optimum doping concentrations. The redshift in the emission spectra at higher doping levels further supports the notion of electronic structure modifications, which could potentially affect charge transport and recombination dynamics.

### 3.4 | PEC Properties

PEC experiments were run in a 1 M NaOH solution, with the addition of a hole scavenger to enhance charge extraction from the photoanode and to prevent surface self-oxidation. It is known that one of the main bottlenecks of  $\text{Ta}_3\text{N}_5$  is the slow charge-transfer mechanism at the solid–liquid interface, where the accumulation of the photogenerated holes leads to oxidation of the surface and passivation of the electrodes [53, 54]. The addition

of a valence hole scavenger like  $\text{K}_4\text{Fe}(\text{CN})_6$  accelerates the extraction of the holes from the photoanode, thus preventing the holes from being consumed through surface oxidation. In particular, by progressively increasing the atomic concentration of Ti in the  $\text{Ta}_3\text{N}_5$  films, there is a clear trend in photocurrent values, which keep increasing up to 2 at% Ti doping, and then decrease again at higher Ti doping (3.5 at%), also the anodic shift in the onset potential under constant light illumination as can be seen in Figure 5a [34]. Furthermore, Figure 5b compares the chopped LSV curves where a seven-fold increase in photocurrent density of 2 at% Ti-doped films can be seen as compared to the undoped one. Interestingly, there are no big differences in the photopotential sustained by these two films under illumination (see Figure 5c). Thus, increased photocurrent value shown by the doped film cannot be then ascribed to a larger photo potential solely [34]. But another key aspect that can be observed in the OCP measurements is the different relaxation time to reach the steady-state situation under dark conditions, Figure 5d. Assuming pseudo-first-order kinetics, this parameter can be quantitatively estimated with the following formula [55]:

$$\tau = \frac{k_B T}{e} \left( \frac{dV_{oc}}{dt} \right)^{-1}$$

where  $k_B$  is the Boltzmann constant,  $T$  is the solution temperature, and  $e$  is the electron charge (the raw portion of the curve used for decay time estimation is reported in the Figure S6). As discussed in the earlier section the 2 at% Ti-doped film shows a much slower decay time as compared to the undoped one. Thus, charge recombination has been greatly reduced by the incorporation of Ti, which is coherent with the observed increased carrier lifetime. Overall, Ti doping has removed defect states which could be responsible for shorter photocarriers lifetime due to the higher recombination rate.

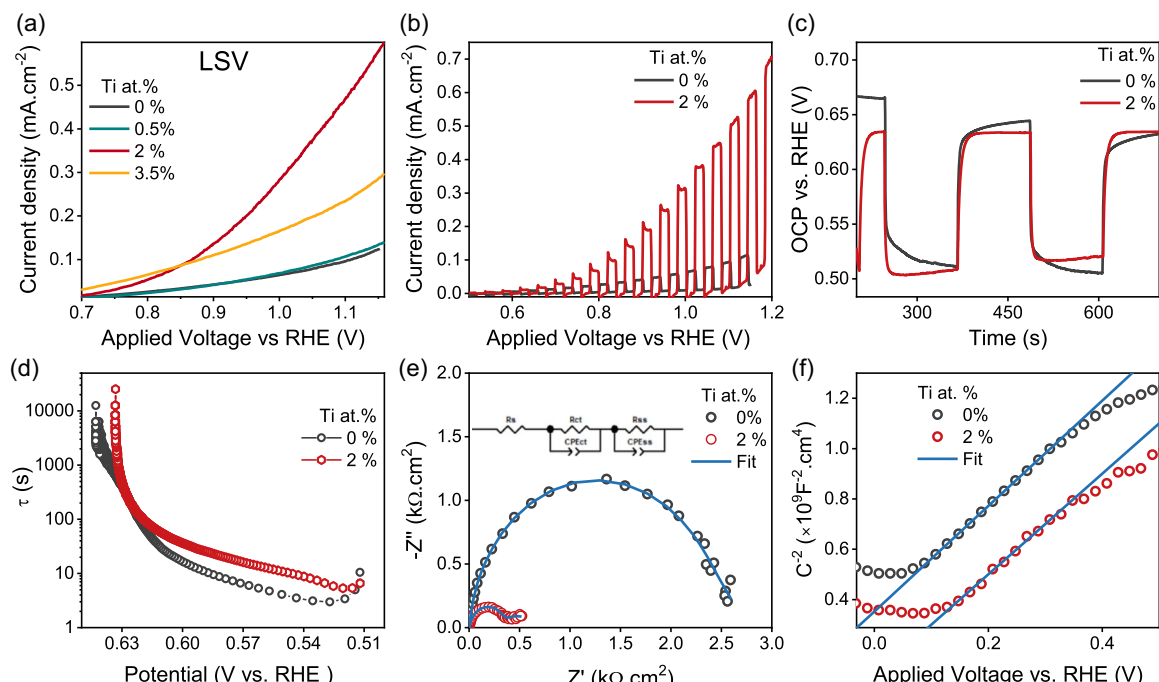


**FIGURE 5** | Photoelectrochemical measurements of Ti-doped  $\text{Ta}_3\text{N}_5$  thin films in pH 12.8 and 0.1 M  $\text{K}_4\text{Fe}(\text{CN})_6$  as a sacrificial reagent. (a) LSV under constant light illumination, (b) chopped LSV comparison, (c) OCP comparison, (d) Decay-time estimated from OCP, (e) Nyquist plot acquired at 0.9 V RHE with inset shows equivalent circuit, and (f) Mott-Schottky plots for 0% and 2% Ti-doped  $\text{Ta}_3\text{N}_5$  films.

Furthermore, the impedance data were fitted with the equivalent circuit in the inset of Figure 5e, and the estimated resistances are reported in Table S4. At low applied potentials, lower than 0.9 V RHE, both space charge resistance ( $R_{ss}$ ) and charge transfer resistance ( $R_{ct}$ ) have comparable values, but  $R_{ss}$  drops much before  $R_{ct}$ , suggesting at intermediate potentials, reaction kinetics is controlled by the charge-transfer velocity at the interface [56, 57]. As compared to the undoped film, both the loops appear to be smaller in the Ti-doped one. Specifically, at 0.9 V RHE, the  $R_{ct}$  and  $R_{ss}$  resistances are 3.4 and 0.4  $\text{k}\Omega \text{cm}^2$ , respectively, in the undoped film, and of 1.4 and 0.4  $\text{k}\Omega \text{cm}^2$  in the doped one. The role of Ti is then particularly evident in the charge-transfer loop, where an easier transfer of holes from the material to the electrolyte is allowed by Ti incorporation. This is the indication of the removal of unfavorable intra band-gap defects, which, behaving as trap states or recombination centers, reduce the efficiency of the film in exploiting photogenerated holes.

Finally, Figure 5f, a Mott-Schottky evaluation of the undoped and 2% Ti-doped film is reported. The flat-band potential is shifted by  $\approx 100$  mV to more anodic potential after the incorporation of Ti, compatible with a down-shift of the  $E_F$  upon removal of the intra-bandgap defects. This aspect does not translate into a significant lower onset potential of photocurrent in the Ti-doped film, likely because of the charge-transfer kinetics being the kinetic bottleneck of the system. All the results from the Mott-Schottky analysis are reported in Table S5.

### 3.5 | Electronic Structure Near $E_F$ and Band Diagram

The schematic band diagram is given in Figure 6, where the band positions are aligned using the VBS and PL results. It shows

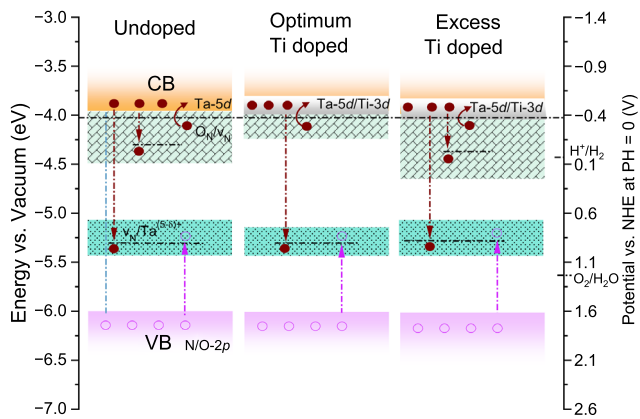


**FIGURE 6** | Schematic band diagram of undoped  $\text{Ta}_3\text{N}_5$ , optimum Ti-doped, and excess Ti-doped  $\text{Ta}_3\text{N}_5$ .

influence of Ti doping on the electronic structure of  $\text{Ta}_3\text{N}_5$  films, particularly with respect to defect states and band structure [14, 20]. As the dominant defects related to  $\text{v}_N/\text{Ta}^{(5-\delta)+}$  and  $\text{O}_N$  related defects are directly visualized VB spectra and supported by the PL measurements. In undoped  $\text{Ta}_3\text{N}_5$ , prominent in-gap defect states exist, which lead to rapid recombination of excitons. Specifically,  $\text{v}_N$ /reduced Ta which reported to be lies below the water reduction potential, thus responsible for reduced PEC [20]. Though the  $\text{Ti}_{\text{Ta}}$  has an electron acceptor character, the VB spectra remain unaltered around VBM. These results are in agreement with recent theoretical work of Fan et al. [15], which shows the associate  $\text{Ti}_{\text{Ta}}-\text{O}_N$  complex introduces a deep transition level. Thus at optimum Ti doping of 2 at%, these defects are significantly minimized due to charge balance  $\text{Ti}-\text{O}$  [13]. However, when the Ti concentration exceeds the optimal level, these defect states reappear, and the band gap begins to shrink due to the emergence of Ti 3d states near the CB minimum, as shown in Figure 6. This not only reintroduces recombination centers but also reduces the efficiency of charge separation and light absorption balance. At higher Ti doping, the emergence of additional defect indicates complex defect interactions and requires detailed theoretical calculations. Overall, the results demonstrate that Ti doping plays a crucial role in controlling defect states, and excessive doping can negatively impact PEC performance and degrade electronic properties.

#### 4 | Conclusion

The present work has yielded important insights into the interplay between structural, optical, and electronic properties. Structural, compositional, and spectroscopy analysis confirms that the films retain the orthorhombic structure even with increasing Ti content up to  $\approx 10$  at%. The systematic lattice contraction along with estimated composition is consistent with the substitution of  $\text{Ta}^{5+}$  by the slightly smaller  $\text{Ti}^{4+}$  ions. Doping-dependent site preference is also observed, where Ti initially favors substitution at Ta coordinated with four-fold N site at low concentrations and shifts to the three-fold N coordinated at higher doping levels. The optimal Ti doping (2 at%) reduces the presence of lower-valence Ta species and stabilizes the  $\text{Ta}_3\text{N}_5$  phase effectively modifying the electronic transitions. At an optimal Ti doping, the near-band-edge emission is

significantly enhanced while defect-related emissions are suppressed, resulting in an extended exciton lifetime compared to the undoped film. This improvement indicates that moderate Ti-O incorporation passivates in-gap defect states, thereby reducing nonradiative recombination and improving carrier dynamics. However, further increase in Ti content leads to increased O content and lattice distortion, reappearance of defect states, and a higher density of nonradiative recombination centers, ultimately impairing PEC performance. Collectively, these findings emphasize the importance of precise doping control. While Ti substitution can beneficially modify the electronic structure and reduce defect-mediated recombination at moderate levels, surpassing the optimal concentration introduces adverse effects that compromise charge transport and overall device performance. These insights provide a pathway for optimizing  $\text{Ta}_3\text{N}_5$ -based materials for advanced PEC applications.

#### Author Contributions

**Shailesh Kalal:** data curation (lead); formal analysis (lead); investigation (lead); methodology (lead); project administration (lead); software (lead); validation (lead); visualization (lead); writing – original draft (lead); writing – review & editing (lead). **Martin Magnuson:** conceptualization (equal); data curation (lead); formal analysis (equal); investigation (equal); methodology (equal); resources (lead); software (lead); validation (equal); visualization (equal); writing – original draft (equal); writing – review & editing (equal). **Alessandro Chesini:** conceptualization (equal); data curation (lead); formal analysis (lead); investigation (equal); methodology (equal); software (lead); validation (lead); visualization (lead); writing – original draft (equal); writing – review & editing (equal). **Akshaya A:** data curation (supporting); investigation (supporting); writing – review & editing (supporting). **Sanath Kumar Honnali:** data curation (equal); formal analysis (equal); methodology (equal); writing – original draft (supporting); writing – review & editing (supporting). **Sophia Sahoo:** formal analysis (supporting); investigation (supporting); validation (supporting); writing – review & editing (supporting). **Nakul Jain:** data curation (supporting); investigation (supporting); methodology (supporting); writing – review & editing (supporting). **Dibyendu Bhattacharyya:** data curation (supporting); resources (lead). **Andrei Gloskovskii:** data curation (equal); formal analysis (supporting); methodology (supporting); resources (lead); writing – review & editing (equal). **Mukul Gupta:** methodology (supporting); resources (equal); validation (supporting). **Feng Wang:** resources (equal); software (supporting); visualization (supporting). **Michele Orlandi:** data curation (equal); formal analysis (equal); investigation (equal); methodology (lead); software (equal); validation (equal); writing – original draft (equal); writing – review & editing (equal). **Grzegorz Greczynski:** formal analysis (supporting); investigation (supporting); methodology (supporting); validation (supporting); writing – review & editing (equal). **Kenneth Järrendahl:** formal analysis (supporting); investigation (supporting); validation (equal); writing – review & editing (supporting). **Per Eklund:** formal analysis (equal); investigation (equal); validation (equal); visualization (equal); writing – review & editing (equal). **Jens Birch:** formal analysis (supporting); resources (equal); validation (supporting). **Ching-Lien Hsiao:** conceptualization (equal); data curation (equal); funding acquisition (lead); methodology (equal); project administration (lead); resources (lead).

#### Acknowledgments

This work was funded by Olle Engkvists Stiftelse (Grant No. 238–0091, 227–0244 and 197–0210, C-L.H.), Swedish Research Council (VR) (Grant No. 2018–04198 (C-L.H.) and 2021–03826 (P.E.)), and Carl Tryggers Stiftelse (Grant No. CTS 24:3577 (C-L.H.), CTS23:2746 (C-L.H.), CTS 22:2029 (M.M.) and CTS20:272 (M.M.)), and the Swedish Energy Research (Grant No. 43606–1, M.M.). The computations were enabled

by resources provided by the Swedish National Infrastructure for Computing (SNIC) at the National Supercomputer Centre (NSC) partially funded by the VR (Grant No. 2016–07213, M.M.). The authors also acknowledge funding from the Swedish Government Strategic Research Area in Materials Science on Functional Materials at Linköping University (Faculty Grant SFO-Mat-LiU No. 2009 00971) and the Knut and Alice Wallenberg Foundation through the Wallenberg Academy Fellows program (KAW-2020.0196, P.E.). The authors gratefully acknowledge Daniel Primetzhofer and Mauricio Sortica for RBS and ToF-ERDA measurements at Tandem Laboratory, Uppsala University which is financed by the Swedish Research Council VR-RFI under contract number 2019–00191. A part of this work is supported through the India-DESY project. S. K. acknowledge Dr. Rajshri Urkude for assisting in XAS measurements. M.O. acknowledges funding from project “Produrre Idrogeno in Trentino—H<sub>2</sub>@TN” (PAT-Trento).

## Funding

This work was supported by the Olle Engkvists Stiftelse (238-0091, 227-0244, 197-0210); Swedish Research Council (2018-04198, 2021-03826); Carl Tryggers Stiftelse (CTS 24:3577, CTS23:2746, CTS 22:2029, CTS 20:272), Swedish Energy Research (43606-1), Swedish National Infrastructure for Computing, National Supercomputer Centre (2016-07213), Swedish Government Strategic Research Area in Materials Science on Functional Materials (2009 00971) and Knut and Alice Wallenberg Foundation (KAW-2020.0196).

## Conflicts of Interest

The authors declare no conflicts of interest.

## Data Availability Statement

The data that support the findings of this study are available from the corresponding author upon reasonable request.

## References

1. N. S. Lewis, “Toward Cost-Effective Solar Energy use,” *Science* 315 (2007): 798.
2. R. E. Blankenship, D. M. Tiede J. Barber, et al., “Comparing Photosynthetic and Photovoltaic Efficiencies and Recognizing the Potential for Improvement,” *Science* 332 (2011): 805.
3. Y. Tachibana, L. Vayssières, and J. R. Durrant, “Artificial Photosynthesis for Solar Water-Splitting,” *Nature Photonics* 6 (2012): 511.
4. R. L. House, N. Y. M. Iha, R. L. Coppo, et al., “Artificial Photosynthesis: Where Are We now? Where Can We Go?,” *Journal of Photochemistry and Photobiology C: Photochemistry Reviews* 25, no. ,32, 2015.
5. R. Daghbir, P. Drogui, and D. Robert, “Modified TiO<sub>2</sub> for Environmental Photocatalytic Applications: A Review,” *Industrial & Engineering Chemistry Research* 52 (2013): 3581.
6. Y. He, J. E. Thorne, C. H. Wu, et al., “What Limits the Performance of Ta<sub>3</sub>N<sub>5</sub> for Solar Water Splitting?,” *Chem* 1 (2016): 640.
7. M. Hojamberdiev, J. M. Mora-Hernandez, R. Vargas, et al., “Time-Retrenched Synthesis of BaTaO<sub>2</sub>N by Localizing an NH<sub>3</sub> Delivery System for Visible-Light-Driven Photoelectrochemical Water Oxidation at Neutral pH: Solid-State Reaction or Flux Method?,” *ACS Applied Energy Materials* 4 (2021): 9315.
8. C. M. Leroy, A. E. Maegli, K. Sivula, et al., “LaTiO<sub>2</sub>N/In<sub>2</sub>O<sub>3</sub> Photoanodes with Improved Performance for Solar Water Splitting,” *Chemical Communications* 48 (2012): 820.
9. R. Kikuchi, T. Nakamura, S. Tamura, Y. Kaneko, and K. Hato, “Fundamental Semiconducting Properties of Perovskite Oxynitride SrNbO<sub>2</sub>N: Epitaxial Growth and Characterization,” *Chemistry of Materials* 29 (2017): 7697.
10. T. Higashi, H. Nishiyama, Y. Otsuka et al., “Efficient Water Oxidation Using Ta<sub>3</sub>N<sub>5</sub> Thin Film Photoelectrodes Prepared on Insulating Transparent Substrates,” *ChemSusChem* 13 (1974): 2020.
11. T. Higashi, H. Nishiyama, Y. Pihosh, et al., “Physicochemical Insights into Semiconductor Properties of a Semitransparent Tantalum Nitride Photoanode for Solar Water Splitting,” *Physical Chemistry Chemical Physics* 25 (2023): 20737.
12. L. Cui, M. Wang, and Y. X. Wang, “Nitrogen Vacancies and Oxygen Substitution of Ta<sub>3</sub>N<sub>5</sub>: First-Principles Investigation,” *Journal of the Physical Society of Japan* 83 (2014): 1.
13. G. Fan, Z. Zhou, Y. Jing, and T. Frauenheim, “Suppression of Charge Carrier Recombination in a Ta<sub>3</sub>N<sub>5</sub> Photoanode via Defect Regulation: A Theoretical Investigation,” *Journal of Materials Chemistry A* 12 (2024): 15922.
14. Y. Xiao, Z. Fan, M. Nakabayashi, et al., “Decoupling Light Absorption and Carrier Transport via Heterogeneous Doping in Ta<sub>3</sub>N<sub>5</sub> Thin Film Photoanode,” *Nature Communications* 13 (2022): 1.
15. G. Fan, X. Wang, H. Fu, J. Feng, Z. Li, and Z. Zou, “Compensation of Band-Edge Positions in Titanium-Doped Ta<sub>3</sub>N<sub>5</sub> Photoanode for Enhanced Water Splitting Performance: A First-Principles Insight,” *Physical Review Materials* 1 (2017): 1.
16. Y. Pihosh, V. Nandal, T. Higashi, et al., “Tantalum Nitride-Enabled Solar Water Splitting with Efficiency Above 10%,” *Advanced Energy Materials* 13 (2023): 2301327.
17. Y. Xiao, C. Feng, J. Fu, et al., Band Structure Engineering and Defect Control of Ta<sub>3</sub>N<sub>5</sub> for Efficient Photoelectrochemical Water Oxidation,” *Nature Catalysis* 3 (2020): 932.
18. J. Fu, Z. Fan, M. Nakabayashi, et al., “Interface Engineering of Ta<sub>3</sub>N<sub>5</sub> Thin Film Photoanode for Highly Efficient Photoelectrochemical Water Splitting,” *Nature Communications* 13 (2022): 1.
19. H. R. Kwon, J. W. Yang, S. Choi, et al., “Low Onset-Potential Z-Scheme Ta<sub>3</sub>N<sub>5</sub>-Based Photoanode with Enhanced Light Harvesting and Charge Transport,” *Advanced Energy Materials* 14 (2024): 1.
20. J. Fu, F. Wang, Y. Xiao, et al., “Identifying Performance-Limiting Deep Traps in Ta<sub>3</sub>N<sub>5</sub> for Solar Water Splitting,” *ACS Catalysis* 10 (2020): 10316.
21. J. Wang, A. Ma, Z. Li, J. Jiang, J. Feng, and Z. Zou, “Effects of Oxygen Impurities and Nitrogen Vacancies on the Surface Properties of the Ta<sub>3</sub>N<sub>5</sub> Photocatalyst: A DFT Study,” *Physical Chemistry Chemical Physics* 17 (2015): 23265.
22. J. Wang, A. Ma, Z. Li, J. Jiang, J. Feng, and Z. Zou, “Effects of Ba-O Codoping on the Photocatalytic Activities of Ta<sub>3</sub>N<sub>5</sub> Photocatalyst: A DFT Study,” *RSC Advances* 4 (2014): 55615.
23. Y. Li, T. Takata, D. Cha, et al., “Vertically Aligned Ta<sub>3</sub>N<sub>5</sub> Nanorod Arrays for Solar-Driven Photoelectrochemical Water Splitting,” *Advanced Materials* 25 (2013): 125.
24. S. Suzuki, M. Yanai, T. Yamada, et al., “Ta<sub>3</sub>N<sub>5</sub> Photoanodes Fabricated by Providing NaCl-Na<sub>2</sub>CO<sub>3</sub> Evaporants to Tantalum Substrate Surface under NH<sub>3</sub> Atmosphere,” *ACS Applied Energy Materials* 1 (2018): 11.
25. Z. Wang, Y. Inoue, T. Hisatomi, et al., “Overall Water Splitting by Ta<sub>3</sub>N<sub>5</sub> Nanorod Single Crystals Grown on the Edges of KTaO<sub>3</sub> Particles,” *Nature Catalysis* 1 (2018): 756.
26. J. W. Yang, H. R. Kwon, S. G. Ji, et al., Conjugated Polythiophene Frameworks as a Hole-Selective Layer on Ta<sub>3</sub>N<sub>5</sub> Photoanode for High-Performance Solar Water Oxidation,” *Advanced Functional Materials* 34 (2024): 1.
27. X. Wang, Q. Zhou, H. Zhang, and Y. Wang, “Epitaxial Growth of a Three-Dimensional Hollow and Chestnut Shell Photothermal p-n Junction Photoanode,” *ACS Nano* 18 (2024): 29794.

28. Y. Liu, Z. Fan, R. Li, et al., "Lattice-Matched  $Ta_3N_5$ /Nb<sub>5</sub>N<sub>6</sub> Interface Enables a Bulk Charge Separation Efficiency of Close to 100%," *ACS Energy Letters* 10 (2025): 1911.

29. J. Seo, T. Takata, M. Nakabayashi, et al., "Mg-Zr Cosubstituted  $Ta_3N_5$  Photoanode for Lower-Onset-Potential Solar-Driven Photoelectrochemical Water Splitting," *Journal of the American Chemical Society* 137 (2015): 12780.

30. J. Xiao, J. J. M. Vequizo, T. Hisatomi, et al., Simultaneously Tuning the Defects and Surface Properties of  $Ta_3N_5$  Nanoparticles by Mg-Zr Codoping for Significantly Accelerated Photocatalytic H<sub>2</sub> Evolution," *Journal of the American Chemical Society* 143 (2021): 10059.

31. X. Wang, H. Zhang, C. Feng, and Y. Wang, "Engineering Band Structuring via Dual Atom Modification for an Efficient Photoanode," *Chemical Science* 15 (2023): 896.

32. J. M. Morbec and G. Galli, "Charge Transport Properties of Bulk  $Ta_3N_5$  from First Principles," *Physical Review B* 93 (2016): 1.

33. X. Wang, H. Huang, J. Wang, Z. Li, and Z. Zou, "Suppression of Point Defects for Band Edge Engineering in a Semiconducting Photocatalyst," *The Journal of Physical Chemistry Letters* 11 (2020): 1708.

34. L. I. Wagner, E. Sirotti, O. Brune, et al., Defect Engineering of  $Ta_3N_5$  Photoanodes: Enhancing Charge Transport and Photoconversion Efficiencies via Ti Doping," *Advanced Functional Materials* 34 (2024): 2306539.

35. J.-C. Chang, J. Palisaitis, S. Kalal, et al., "The Role of a  $Ta_2O_5$  Seed Layer on Phase Evolution and Epitaxial Growth of  $Ta_3N_5$  Thin Films on Al<sub>2</sub>O<sub>3</sub>(0001)," *ACS Applied Energy Materials* 8 (2025): 6699.

36. J. C. Chang, J. Birch, G. K. Gueorguiev, et al., Domain Epitaxial Growth of  $Ta_3N_5$  Film on c-Plane Sapphire Substrate," *Surface and Coatings Technology* 443 (2022): 128581.

37. J. C. Chang, F. Eriksson, M. A. Sortica, et al., "Orthorhombic  $Ta_3-xN_5-yOy$  Thin Films Grown by Unbalanced Magnetron Sputtering: The Role of Oxygen on Structure, Composition, and Optical Properties," *Surface and Coatings Technology* 406 (2021): 126665.

38. P. Ström and D. Primetzhofer, "Ion Beam Tools for Nondestructive in-Situ and in-Operando Composition Analysis and Modification of Materials at the Tandem Laboratory in Uppsala," *Journal of Instrumentation* 17 (2022): 34-41.

39. K. Arstila, J. Julin, M. I. Laitinen, et al., "Potku - New Analysis Software for Heavy Ion Elastic Recoil Detection Analysis," *Nuclear Instruments and Methods in Physics Research Section B: Beam Interactions with Materials and Atoms* 331 (2014).

40. B. Ravel and M. Newville, "ATHENA, ARTEMIS, HEPHAESTUS: Data Analysis for X-Ray Absorption Spectroscopy Using IFEFFIT," *Journal of Synchrotron Radiation* 12 (2005): 537.

41. C. Schlueter, A. Gloskovskii, K. Ederer, et al., "The New Dedicated HAXPES Beamline P22 at PETRAIII," in *AIP Conference Proceedings*, 2054, (AIP Publishing, 2023), 040010.

42. P. E. Blöchl, "Projector Augmented-Wave Method," *Physical Review B* 50 (1994): 17953.

43. G. Kresse and J. Hafner, "Ab Initio Molecular Dynamics for Liquid Metals," *Physical Review B* 47 (1993): 558.

44. A. I. Liechtenstein, V. I. Anisimov, and J. Zaanen, "Strong Interactions: Orbital Ordering," *Physical Review B* 52 (1995): 5467.

45. M. A. Gluba and N. H. Nickel, "Transition-Metal Acceptor Complexes in Zinc Oxide," *Physical Review B* 87 (2013): 1.

46. A. Janotti, D. Segev, and C. G. Van De Walle, "Effects of Cation d States on the Structural and Electronic Properties of III-Nitride and II-Oxide Wide-Band-Gap Semiconductors," *Physical Review B* 74 (2006): 1.

47. P. Scherrer, *Bestimmung Der Inneren Struktur Und Der Größe Von Kolloidteilchen Mittels Röntgenstrahlen*, in *Kolloidchemie Ein Lehrbuch* (Springer Berlin Heidelberg, 1912), 387-409.

48. Z. G. Yuan, S. Zhao, F. H. Liu, J. Li, Z. Y. Wang, and J. P. Wang, "Exploring the Influence of Grain Boundaries on Carrier Transport and PEC Activity of Hematite Photoelectrodes," *ACS Applied Energy Materials* 8 (2025): 8579.

49. S. Kalal and M. Gupta, *3-Comparative Study of Transition Metal Nitride Thin Films Grown Using DcMS and HiPIMS*, (Elsevier Ltd., 2025).

50. S. Kalal, Y. Kumar, S. Karmakar, et al., "Study of Niobium Mononitride Thin Films Grown Using High Power Impulse Magnetron Sputtering," *Physica Status Solidi (RRL) - Rapid Research Letters* 16 (2022): 1.

51. L. M. Wolz, G. Grötzer, T. Rieth, et al., "Impact of Defects and Disorder on the Stability of  $Ta_3N_5$  Photoanodes," *Advanced Functional Materials* 2405532 (2024): 1.

52. S. Kalal, A. Tayal, S. Karmakar, R. Joshi, et al., "Electron-Phonon Interactions and Superconductivity of  $\beta$ -Nb<sub>2</sub>N Thin Films," *Applied Physics Letters* 122 (2023): 072602.

53. S. Y. Chae and E. D. Park, "Enhanced Photoelectrochemical Stability of  $Ta_3N_5$  in the Acidic Electrolyte Conditions," *Applied Surface Science* 583 (2022): 152566.

54. K. Li, B. Miao, W. Fa, et al., "Evolution of Surface Oxidation on  $Ta_3N_5$  as Probed by a Photoelectrochemical Method," *ACS Applied Materials & Interfaces* 13 (2021): 17420.

55. A. Zaban, M. Greenshtein, and J. Bisquert, "Determination of the Electron Lifetime in Nanocrystalline Dye Solar Cells by Open-Circuit Voltage Decay Measurements," *Chemphyschem* 4 (2003): 859.

56. R. L. Doyle and M. E. G. Lyons, "An Electrochemical Impedance Study of the Oxygen Evolution Reaction at Hydrous Iron Oxide in Base," *Physical Chemistry Chemical Physics* 15 (2013): 5224.

57. A. C. Lazanas and M. I. Prodromidis, "Electrochemical Impedance Spectroscopy—A Tutorial," *ACS Measurement Science Au* 3 (2023): 162.

## Supporting Information

Additional supporting information can be found online in the Supporting Information section. **Supporting Fig. S1:** (a) and (b) shows the RBS and Time-of-Flight ERDA profiles of the undoped  $Ta_3N_5$ . (c) and (d) RBS and ERDA profiles of 2 at% Ti doped  $Ta_3N_5$  thin films. **Supporting Fig. S2:** SEM images of (a) undoped and (b) 2 at% Ti-doped  $Ta_3N_5$  thin films with insets showing the respective cross-section images. Both samples retain similar morphology indicating homogenous doping of Ti within the  $Ta_3N_5$  matrix. The cross-section images show the columnar growth of films. **Supporting Fig. S3:** Fitted XPS core-level spectra of (a) Ta 4f (b) N 1s (c) O 1s of pristine and Ti-doped  $Ta_3N_5$  thin films for undoped, Ti doping level of 2 at% and 3.5 at%. All the spectra are fitted using CASAXPS software using Shirley background and combination of GL(30) peak functions. **Supporting Fig. S4:** Ti-2p core-level HAXPS spectra on the  $Ta_3N_5$  thin films for Ti doping of 0.5, 2, 3.5 and 10 at%. No detectable Ti signal appears at the lowest doping level of 0.5 at%. However, at higher Ti doping contents (2, 3.5, and 10 at%), a broad Ti 2p<sub>3/2</sub> peak emerges at shoulder of Ta 4p<sub>1/2</sub> peak. **Supporting Fig. S5:** UV-vis absorption spectra of  $Ta_3N_5$  thin films with Ti doping of 0, 0.5, 2, 3.5 and 10 at%. Inset compares the raw absorbance spectra with simulated data after removal of interference oscillations at low energy. **Supporting Fig. S6:** Zoom on the raw data used for estimating the OCP decay time. The corresponding formula from the manuscript was directly applied to the raw curve, by numerically estimating the derivative. **Supporting Table S1:** Composition analysis via RBS/ERDA of the  $Ta_3N_5$  thin films grown at various Ti power. All the samples contain approx. 2 at% argon which is not listed and normalized to get the atomic composition. The crystallite size (CS) is measured using the Sherrer's

formula  $d = 0.9\lambda/\beta\cos(\theta)$ , where  $\lambda$  is the wavelength of incident X-ray,  $\beta$  is the FWHM of the (023) reflection and  $\theta$  is the corresponding angle.

**Supporting Table S2:** Quantitative composition analysis Ta in the form of reduced Ta species ( $\text{Ta}^{(5-6)+}$ ),  $\text{Ta}_3\text{N}_5$  ( $\text{Ta}^{5+}$ ), and oxygen substituted  $\text{Ta}_3\text{N}_5$  (TaON) for undoped and the 2 and 3.5 at% Ti doped  $\text{Ta}_3\text{N}_5$  thin films. **Supporting Table S3:** Fitted parameters for the TRPL decay curve of Ti-doped  $\text{Ta}_3\text{N}_5$  thin films. To extract the average electron-hole recombination lifetime. TRPL decay curves were fitted using the biexponential equation using FAST Version 3.5.0 Edinburgh Instruments. The  $f_1$  and  $f_2$  are the fractional intensities;  $\tau_1$  and  $\tau_2$  are the lifetimes;  $\bar{\tau}$  is the intensity-weighted average lifetime, which is equal to  $f_1\tau_1 + f_2\tau_2$ ; and  $\chi^2$  is the reduced chi-square value. **Supporting Table S4:** Fitted parameters from EIS impedance spectra, by using the equivalent circuit in Figure 5(e). **Supporting Table S5:** Flat potential, carrier concentration and space-charge width as extracted by fitting the linear region of the Mott-Schottky plot.